# Quantification of Motion-Induced Measurement Error on Floating Lidar Systems

Felix Kelberlau[1] and Jakob Mann[2]

[1]Fugro Norway AS, Havnegata 9, 7462 Trondheim, Norway
[2]DTU Wind, Technical University of Denmark, 4000 Roskilde, Denmark

**Correspondence:** Felix Kelberlau (f.kelberlau@fugro.com)

**Abstract.** Floating lidar systems (FLS) are widely used for offshore wind site assessment and their measurements show good agreement when compared to trusted reference sources. Though, some influence of motion on mean wind speed data from FLS has to be assumed but could not have been quantified with experimental methods yet because the involved uncertainties are larger than the expected impact of motion. This study describes the motion-induced bias on horizontal mean wind speed estimates from FLS with the help of simulations of the lidar sampling pattern of a continuous-wave (CW) velocity-azimuth display (VAD) scanning wind lidar. Analytic modelling is used to validate the simulations. It is found that the error depends on amplitude and frequency of tilt motion, the relative angle between wind direction and tilt motion, and the strength of wind shear. The results are used to quantify the measurement deviation that is caused by motion for the example of the Fugro SEAWATCH Wind LiDAR Buoy (SWLB) carrying a ZX 300M lidar. For the test case of "normal" wave conditions, the bias is as low as 0.04% and for "strong" waves the estimated error is -0.14% of the measurement value. The reason for these low errors lies in a fortunate combination of the frequencies of lidar prism rotation and tilt motion.

## 1 Introduction

Commercially available profiling wind lidars are accurate instruments for measuring mean wind speed and direction onshore in non-complex terrain and offshore (Emeis et al., 2007; Smith et al., 2006; Gottschall et al., 2012). Offshore, in many cases lidars are mounted on floating platforms to avoid the costs for the construction of expensive fixed platforms. When uncorrected lidar measurements from such floating lidar systems (FLS) are compared to values from fixed lidar systems of the same type, several effects can be observed: First, wind direction estimates are influenced by the heading of the FLS (Gottschall et al., 2014). Second, measurements of second order statistics (e.g., turbulence intensity) are higher because the motion of the platform adds to the measured wind speed variance (Kelberlau et al., 2020; Gutiérrez-Antuñano et al., 2018; Désert et al., 2021). The acquired measurements of the horizontal mean wind speed, though, appear to be unbiased. In other words: The motion-induced measurement error is so small that it lies well within the overall uncertainty of experimental trial setups. A more comprehensive understanding of the potential mean wind speed measurement error is crucial for wind site assessment due to the cubic relationship between wind speed and wind turbine electricity production.

Commercial deployments of different types of FLS next to meteorological masts demonstrate good agreement with reference
25  data (Stein et al., 2015; DNV GL, 2019). Linear regression analyses according to the Carbon Trust Roadmap (Carbon Trust,
2018) show slopes close to unity as well as offsets around zero. Furthermore, classification trials of the Fugro SEAWATCH
Wind LiDAR Buoy (SWLB) showed no significant sensitivity of its measurement error to environmental variables such as
wave height or buoy motion parameters. This is also reported for the Fraunhofer IWES LiDAR buoy (Wolken-Möhlmann and
Gottschall, 2020). Gottschall et al. (2017) point out that, in general, sensitivity studies show no significant influence of wave
30  conditions on the accuracy of wind speed measurements from FLS. But they add that the motion-induced measurement error
might be hidden by the larger uncertainty of the reference instruments.

Several studies investigate the error of mean wind speed measurements by FLS with computer simulations. An early example
of such a study is Wolken-Möhlmann et al. (2010). They conclude that the motion-induced measurement error on mean wind
speeds is not negligible and depends on the wave heights, and the error can lead to both over- or underestimation of 10 minute
35  averaged wind speeds. They also point out that the error is caused by rotation rather than translation. Schlipf et al. (2012)
present a different simplified simulation of lidar measurements under the influence of motion. In that study the lidar is assumed
to follow the wave surface and only two non-zero degrees of freedom are considered which leads to significant deviations
from the behaviour of real FLS. The simulations performed by Bischoff et al. (2015) emphasize the effect of wind shear in a
non-uniform flow field but are not realistic enough to quantify the measurement error of real FLS. The more recent study by
40  Salcedo-Bosch et al. (2021) gives a description of measurement error caused by motion in all six degrees of freedom and finds
that it depends on the initial scan phase of the velocity-azimuth display (VAD) scan. Unfortunately, they do neither calculate
the error based on the assumption of randomly distributed initial scan phase angles nor include the effect of wind shear in their
model. Désert et al. (2021) consider the bias on mean wind speeds in their investigation of the effects of motion on turbulence
estimates with a Doppler beam swinging wind lidar.

45  Mangat et al. (2014) show the influence of static tilt under consideration of realistic wind shear conditions both theoreti-
cally and experimentally. Rutherford et al. (2013) and Pitter et al. (2014) extend the same assumptions to the motion of FLS
but ignore the dynamic behaviour of the lidar scanning pattern entirely and therefore oversimplify the measurement error
computation of FLS compared to fixed lidar systems of the same type.

A different approach to isolate the effect of motion in an experiment is to mount a wind lidar on a motion platform and
50  compare the measurements to values from a closely collocated fixed lidar system of the same type. Hellevang and Reuder
(2013) present their results for two different lidar types (WindCube and ZephIR) and various motion cases. The chosen motion
patterns are unfortunately not typical for FLS and the test duration of each case is so short that a quantification of the motion-
induced measurement error is not possible. Tiana-Alsina et al. (2015) employ a ZephIR lidar in different scenarios but also
only for short periods of time, which makes statistically relevant assessments of the small motion-induced error difficult. Also
55  Bischoff et al. (2018) report difficulties that might be caused by the limited amount of experimental data.

The study presented here quantifies the motion-induced error (i.e., bias) on estimates of mean wind velocity measured by a
FLS theoretically. Computer simulations were used to imitate the measurement principle of a FLS carrying a VAD scanning
profiling wind lidar like, the ZX 300M by ZX lidars (Ledbury, United Kingdom). Analytic modelling supports these computer

simulations. The bias was analyzed for measurements at different elevations, under varying wind shear conditions, and for
60 multiple motion states characterized by amplitude and frequency of sinusoidal tilt motion in pitch and roll degrees of freedom
(DoF). We then determined the bias for the example of the SEAWATCH Wind LiDAR Buoy (SWLB) by Fugro (Trondheim,
Norway) under the influence of normal and strong wave conditions.

  Next, section 2 presents how this lidar simulator works and gives basic information about the SWLB. In section 2.3, we
describe how motion influences the reconstructed wind vectors and resulting mean wind velocity estimates of FLS with an
65 without consideration of wind shear. For the example of the SWLB, we define realistic test cases in section 3 and present the
resulting bias. In section 4 we discuss the findings of this study.

## 2 Materials and Methods

### 2.1 Lidar simulator

For computations in this study we developed a lidar simulator that works as follows. In a first step, a power law wind profile is
70 calculated from a reference wind velocity at a reference height and the wind shear coefficient.

  Then a linear time vector is generated with a duration $P = 600$s and a step size of 20ms. For this time vector motion data is
generated based on a sine function with given amplitude and frequency.

  The lidar line-of-sight (LoS) data consist of a time, phase, and LoS velocity vector. The time vector is identical to the time
vector of motion. The vector of lidar prism phase angles consists of 600 full revolutions from 0 to $2\pi$, so that one revolution
75 per second is simulated. This corresponds to the lidar prism rotation frequency of the ZX 300 lidar series. With the help of
the vector transformations presented in Kelberlau et al. (2020), the real azimuth and elevation angle as well as the actual
measurement elevation are calculated for each LoS beam from the prism phase angle, the motion data, and the configured
measurement elevation. From this geometry information, the LoS velocities for each beam are generated by projecting the
height dependent wind velocity vector onto a unit vector pointing into the LoS direction. From this set of synthetic lidar data
80 600 wind vectors are then reconstructed by least-squares figure-of-eight fitting as described for example in Kelberlau and Mann
(2019).

  From Salcedo-Bosch et al. (2021), we know that the phase angle of the first beam in each VAD scan cycle has a strong
impact on the reconstructed wind vector. In order to remove the dependency of the reconstructed mean wind velocity on the
first phase angle, we run each test case 100 times, each time with a phase offset of $\frac{2\pi}{100}$ from the previous run. The average of
85 all these runs will give us the correct bias because the first phase angle is independent of the phase of motion, and each of them
occurs with equal probability.

### 2.2 SEAWATCH Wind LiDAR Buoy

The SEAWATCH Wind LiDAR Buoy by Fugro is a FLS carrying a ZX 300M VAD scanning continuous-wave profiling
wind lidar. It has been deployed for commercial projects around the world. Most of the collected data is used for offshore

**Table 1.** Key parameters of the SEAWATCH Wind LiDAR Buoy by Fugro Norway AS

| Parameter | Value | Unit |
|---|---|---|
| Diameter | 2.8 | [m] |
| Mass | 2200 | [kg] |
| Lidar window height a.s.l. | 1.8 | [m] |

90  wind site assessments where the SWLB measures parameters like mean wind speeds and directions, wave conditions, water current speeds, and atmospheric parameters like temperature and humidity. Measurement campaigns usually last around 12 months for capturing seasonal effects. The SWLB is rated Stage 3 according to the Carbon Trust Roadmap for the Commercial Acceptance of Floating LiDAR Technology (Carbon Trust, 2018), which implies that at least two different SWLB units were classified against at least two different meteorological masts and several other validation trials against trusted reference sources

95  were successfully conducted. A picture and some key parameters of the SWLB are given in Figure 1 and Table 1.

**Figure 1.** Fugro SEAWATCH Wind LiDAR Buoy

## 2.3 Lidar measurements under the influence of motion

## 2.4 Lidar motion in six degrees of freedom

Motion is the single characteristic that differentiates a floating from a fixed lidar system at the same location. That means systematic measurement deviations of a FLS in comparison to a fixed lidar system must be caused by its motion. We assume
100    that this motion is restricted in two ways. First, the translational motion has to be limited to displacement around a fixed point. This assumption is true for FLS that are anchored to the seabed but violated for ship-based lidar systems. Ship-based lidar systems are therefore not covered in this study. The second assumption is that the amplitude of tilt motion of the FLS never exceeds the value at which a lidar beam is horizontal. That means for the investigated lidar system with a half-cone opening angle of $30°$, the tilt amplitude must not exceed $60°$.

105    The rotating prism of the lidar system serves as point of reference for the definition of six motion DoF. We define them as follows:

- Surge: Horizontal motion in mean wind direction

- Sway: Horizontal motion orthogonal to mean wind direction

- Heave: Vertical motion

110    - Roll: Tilt motion around surge axis (tilt leaning perpendicular to wind direction)

- Pitch: Tilt motion around sway axis (tilt leaning in wind direction)

- Yaw: Rotation around vertical axis (heading)

Aligning the surge direction with the wind direction as done in the above definition makes it possible to disregard the wind direction in this study.

115    Lidar motion in the three translational DoF influences the lidar estimates of instantaneous wind velocity. However, as long as the motion is restricted to fluctuations around a fixed point its bias on mean wind speed is zero. Translational motion is therefore disregarded in this study. Instead, the effect of rotational motion in pitch, roll, and yaw has to be analyzed in detail.

## 2.5 Pitch motion with no wind shear

Tilt motion, i.e., inclination of the FLS from the zenith, should be looked at separately for the pitch and roll DoF. First, we will
120    analyse the effect of pitch motion, i.e., rotation of the FLS around a horizontal axis perpendicular to the inflow wind direction.

The influence of static pitch that could be caused by steady forces as from tidal current, wind load, or asymmetric mass distribution on the floating platform is comparably easy to estimate. The effect of a tilted buoy in horizontal flow is identical to the effect of an upright FLS in tilted flow. In this situation some of the horizontal component of the wind is interpreted as vertical inflow component. In accordance with the tilted measurement cone depicted in blue in Figure 2, the error caused by a

125    static pitch angle $\varphi_s$ is

$$\Delta \boldsymbol{u_s} = \cos \varphi_s - 1. \tag{1}$$

Assuming that the static tilt angle $\varphi_s$ will be less than a few degrees under normal operating conditions, the resulting effect of static pitch is low.

    Larger pitch amplitudes are caused by water waves that lead to dynamic rotation of a FLS around its horizontal axes. For
130    dynamic pitch, both the amplitude of motion $A$ and its frequency $f_p$ relative to the VAD scanning frequency $f_s$ are important. ($f_s$=1 Hz in the case of the frequently used ZX 300M.)

    For pitch fluctuations that occur with a very low frequency $f_p \ll f_s$ the pitch angle is nearly constant during the period of each entire scanning cycle (1s) and the lidar measurement cone can be assumed frozen. A visualization is shown in Figure 2. The pitch angle alternates slowly over the course of many scan cycles between $+A$ (blue) and $-A$ (yellow). In these situations
135    the lidar unit will measure too low horizontal velocities because according to Equation 1, $\Delta \boldsymbol{u} < 0$ for $\varphi \neq 0$. The measurement bias

$$\Delta \boldsymbol{u} = \frac{1}{\pi} \int_0^\pi \cos \left( A \sin x \right) dx - 1 \tag{2}$$

can be calculated using

$$\Delta \boldsymbol{u} = J_0(A) - 1 \tag{3}$$

140    where $J_0(A)$ is the Bessel function of the first kind and $A$ is the amplitude of the harmonic pitch oscillation. The solutions for three different pitch amplitudes $A =5°$, $10°$, and $15°$ are visible in Figure 6 for zero tilt frequency.
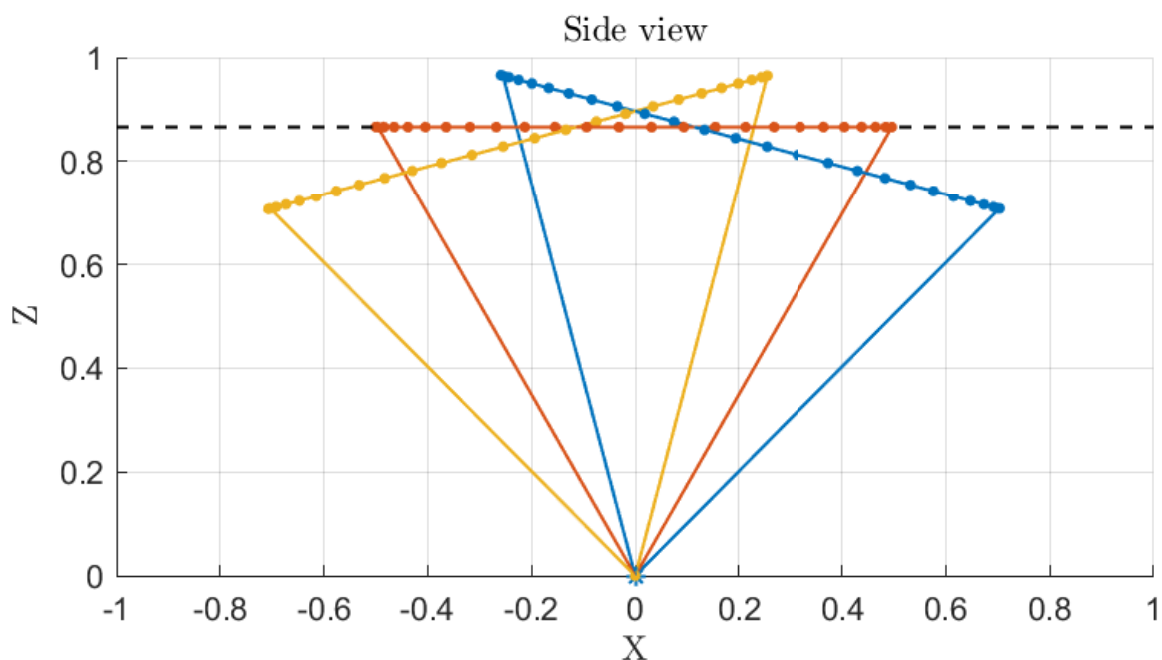
**Figure 2.** Measurement cone under influence of static or slowly changing pitch angle of $A = 20°$ with maximum positive (blue), zero (red), and maximum negative elongation (yellow). Only up- and downwind beams depicted as lines; for other beams focus locations are given by dot markers along measurement circle. Nominal measurement elevation shown (black dashed line).

The situation is different for pitch motion that fluctuates with a frequency $f_p$ close to $f_s$. If $f_p = f_s$ the scanning "cone" for one prism rotation is no longer cone-shaped. If, e.g., the lidar beam pointing in upwind direction is pitched towards the horizon, also the lidar beam pointing in the opposite downwind direction 0.5s later will be pitched towards the horizon. It is

145 equally likely that these two particular beams are pitched towards the zenith or point into their unpitched direction. These three cases are visualized in Figure 3 in blue, yellow, and red respectively.
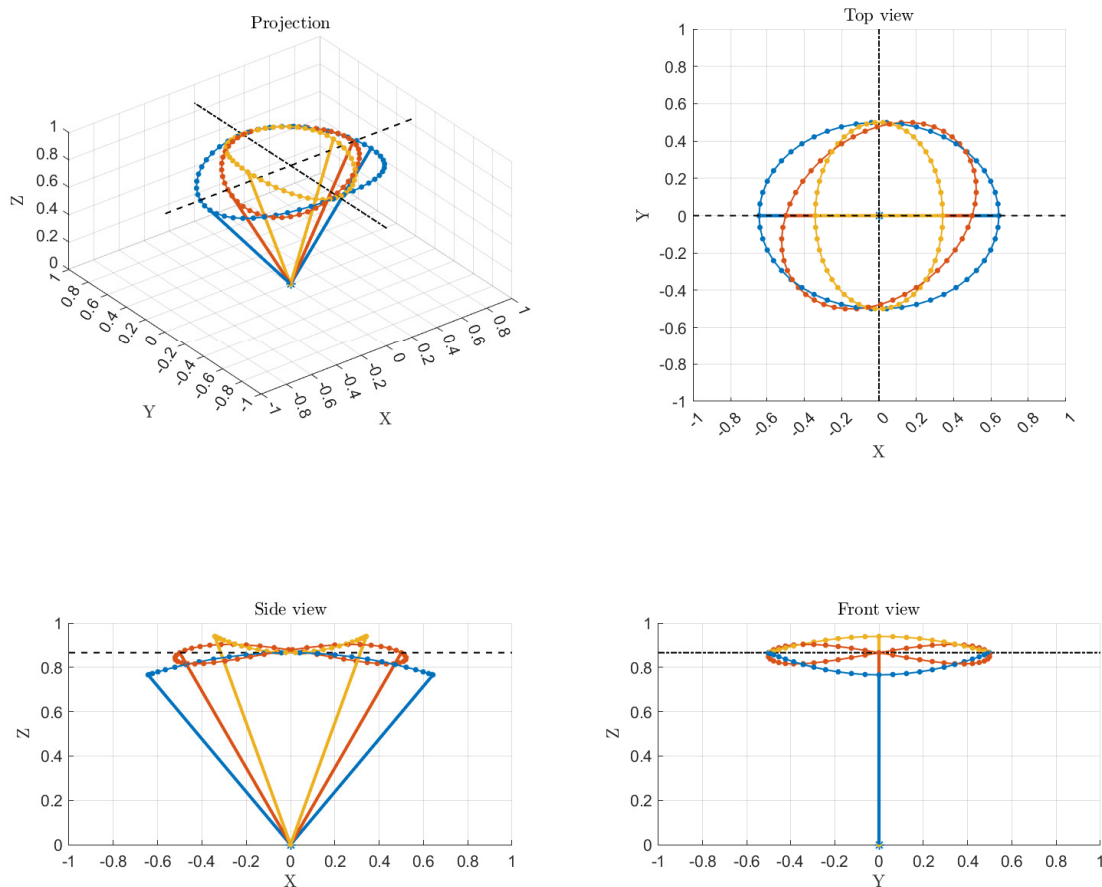
**Figure 3.** Measurement cone under influence of pitch motion with oscillation frequency $f_p = f_s = 1\,\mathrm{Hz}$ and amplitude $A = 10°$. Colors represent different phase shifts between lidar prism angle and pitch motion. Only up- and downwind beams are depicted. The nominal measurement elevation is shown (black dashed line).
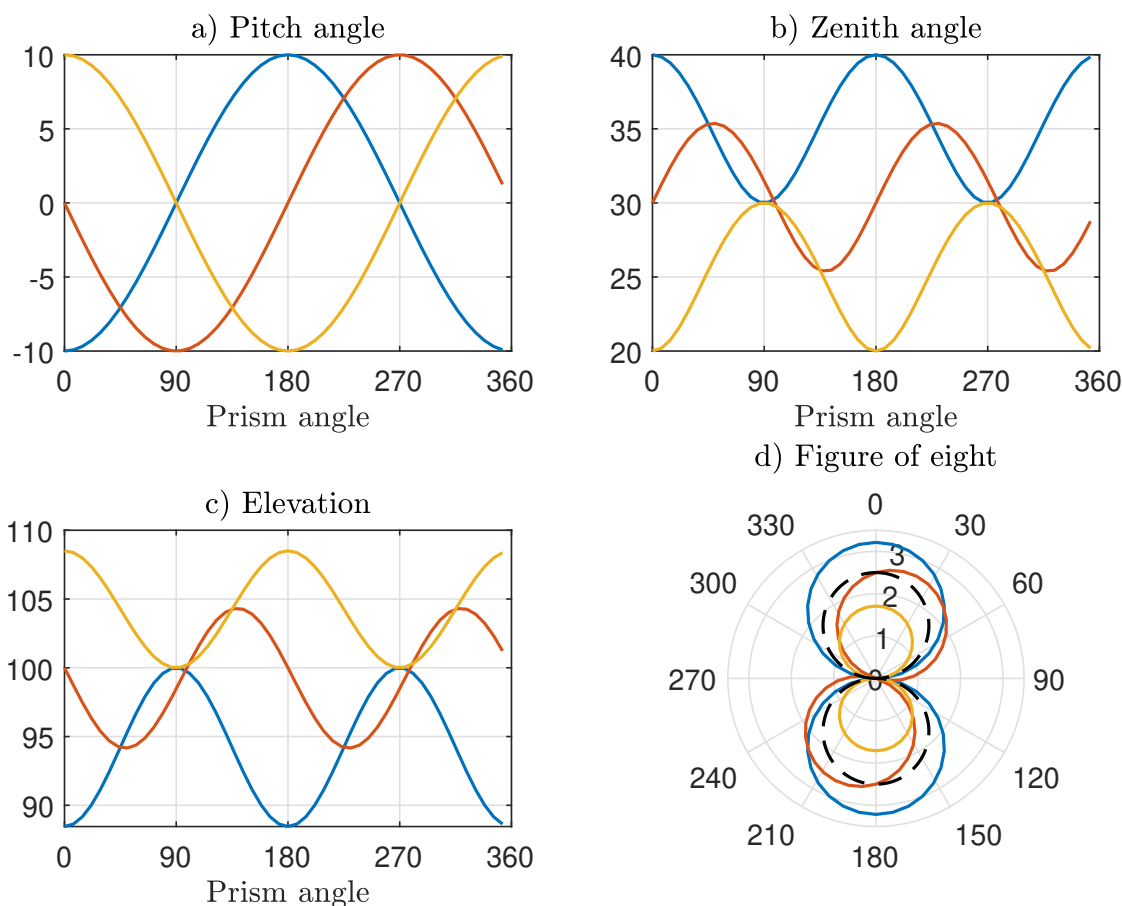
**Figure 4.** Beam geometry of VAD scanning wind lidar under influence of pitch motion with oscillation frequency $f_p = f_s = 1\text{Hz}$ and amplitude $\alpha = 10°$. The subfigures show (**a**) instantaneous pitch angles, (**b**) zenith angles, (**c**) measurement elevations, and (**d**) corresponding figures-of-eight. Colors represent different phase shifts between lidar prism angle and pitch motion corresponding to the colors in Figure 3. Figure-of-eight for fixed lidar is also shown (black dashed).The nominal measurement elevation is 100m.

Figure 4 shows plots of the most important geometrical information for these three cases. Which of them occurs depends on the phase offset between the prism angle (i.e., the lidar phase angle) and the pitch angle. The phase offset between the cases with tilt towards horizon (blue), no tilt (red), and tilt towards zenith (yellow) is 90° each. Plot a) in Figure 4 shows

150 that if for example the beam pointing into upwind direction (blue, prism angle= 0°), is pitched by -10°, the opposing beam in downwind direction (blue, prism angle= 180°) is pitched by +10°. Plot b) shows that in this case the zenith angle, i.e., the angle between the vertical and the beam direction is 40° (blue, prism angle= 0° and 180°). This is the unpitched zenith angle plus one amplitude (the half cone opening angle $\phi = 30°$ plus 10°). Only for the beams pointing perpendicular to the

wind direction (blue, prism angle= $90°$ and $270°$) the zenith angle equals the half cone opening angle. Plot c) shows how
155 the measurement elevation which in this example is set to 100m is influenced by the varying zenith angles. Zenith angles of
more than the half cone opening angle lead to measurements at less than 100m above ground. In this example no wind shear
is assumed and therefore the measurement elevation has no influence on the LoS velocity estimates that are shown in the polar
plot d). The figure-of-eight that corresponds to a fixed lidar measuring the reference wind speed is included as a dashed black
line. It can be seen that the figures-of-eight representing a FLS under the influence of pitch motion in sync with the prism
160 frequency vary substantially depending on the phase shift between motion and lidar prism angle. As expected, the wind speed
estimates are significantly larger if the beams pointing in up- and downwind direction have a larger zenith angle (blue) than
when their zenith angle is reduced by the pitch motion (yellow). But even in the case of zero pitch for the up- and downwind
beams (red), the reconstructed wind vectors are slightly increased (and the wind direction estimate is erroneous).

These three example cases were chosen because they are particularly intuitive to understand. All other possible phase offsets
165 between lidar prism and motion must also be considered. The FLS simulator used in this study is set up to estimate the average
of 100 phase shifts separated by $3.6°$ each. Figure 5 shows the relative measurement error of reconstructed wind vectors as
a function of this phase offset (black dots). The three example cases are marked by vertical lines in yellow, red, and blue
respectively. Since each phase offset is equally likely to occur, the expected error for the mean wind speed is the average of
all possible instantaneous measurement errors (black horizontal line). This expected error is 1.5%. That means a FLS pitching
170 in sync with the lidar prism frequency will overestimate the mean wind speed slightly when no wind shear is present. The
histogram in the lower part of the figure shows that the largest negative errors are larger ($< -0.3$) than the largest positive
errors ($< 0.3$). But this effect is overcompensated by large positive errors being more frequent than large negative errors. For
clarity, the histogram is based on 10,000 evenly distributed phase offset angles.
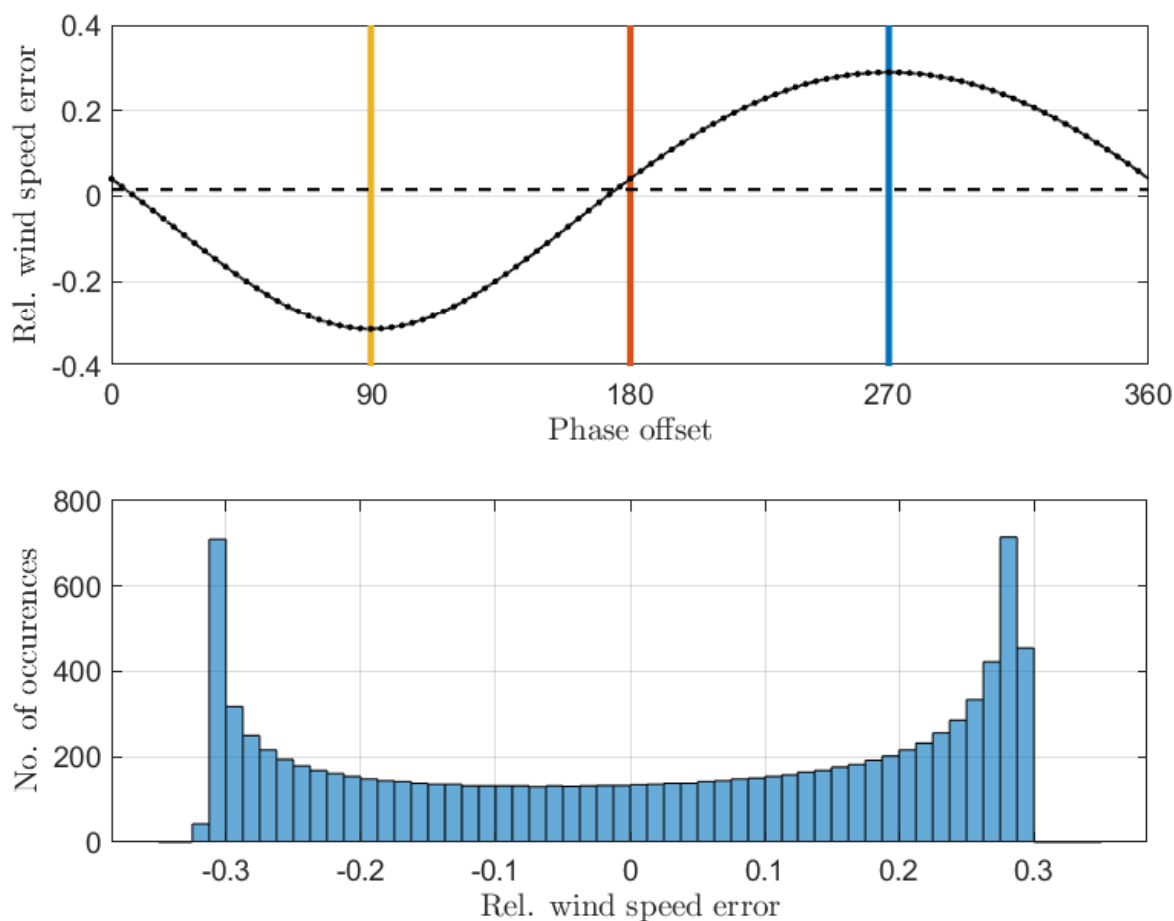
**Figure 5.** (**Top**)Relative motion-induced measurement error caused pitch motion with oscillation frequency $f_p = f_s = 1$Hz and amplitude $\alpha = 10°$ as function of phase offset between lidar prism angle and motion (dot markers). Colored vertical lines mark three particular cases as in Figs. 3-4. Small non-zero bias marked by dashed horizontal line. (**Bottom**) Histogram showing distribution of positive and negative wind speed errors.

In a real world application, dynamic tilt of a FLS occurs neither with very low frequency ($f_p \ll f_s$), nor with exactly the
175 lidar prism frequency ($f_p = f_s$). The motion-induced error must therefore be determined as a function of the frequency of
motion. To achieve this, we configured the simulator to estimate the motion-induced bias for three different pitch amplitudes
($5°$, $10°$, and $15°$) and for a range of motion frequencies (0 Hz...2 Hz). Figure 6 shows the results of these computations.

It can be seen that as predicted in Eq. 3 the bias for motion with very low frequency is negative and as shown in Fig. 5 the
bias at 1 Hz is positive. The largest positive biases are found at $f_p \approx 0.84$ Hz. Overall, the measurement error depends strongly
180 on the amplitude of pitch motion. It is important to point out that in the transition from negative errors at low frequencies to

positive errors at higher frequencies, there is one frequency close to 0.3 Hz at which the bias disappears. This frequency of zero bias is independent of the motion amplitude. The second frequency of zero bias at around 1.5 Hz is of no practical relevance as such high tilt frequencies do not occur for current FLS (see section 3.1). The tilt motion frequency of a FLS is type specific and determined by its mass and hydrodynamic stiffness. From this visualization it is understood that for a FLS with a half cone

185   opening angle of 30° and a prism frequency of 1 Hz in the absence of wind shear, the tilt frequency should be close to 0.3 Hz in order to minimize its bias on mean wind speed estimates.

The overestimation of mean wind speed around $f_p = 0.84$ Hz is caused by the use of scalar averaging for estimating the mean wind speed. The positive bias and strong frequency dependency disappears if vector averaging of the reconstructed wind vectors is applied. Anyway, we recommend using scalar averaging because of its near-zero error at tilt frequencies around

190   0.3 Hz, which is independent of the amplitude of motion.

In Appendix A we present an analytic model for the calculation of the motion-induced error on mean wind speed estimates from a FLS. Results from this analytic solution are included in Figure 6. The purpose of comparing both methods is to validate the simulation results. Overall, the results from both methods agree well. Though, for pitch motion at higher frequencies ($> 1.5$ Hz) the results differ. While the analytic solutions converge towards $J_0(A) - 1$ the simulation results do not. This

195   deviation can be traced back to Eq. A8 in which we allow signed LOS velocities while in the simulator only absolute values of LOS velocities are processed (as in the ZX 300 lidar). At high frequencies of motion where the largest deviations from the ideal figure-of-eight occur this difference has its strongest impact. At lower tilt frequencies some deviation is seen for high amplitudes of motion. This can be explained by the expansion of $A$ to the second order (see Eqs. A12-A13). Expanding $A$ to a higher order would probably eliminate these small deviations. The otherwise close agreement between the results of simulation

200   and model support the assumptions that the simulator works well and that it can be used to predict measurements from FLS.
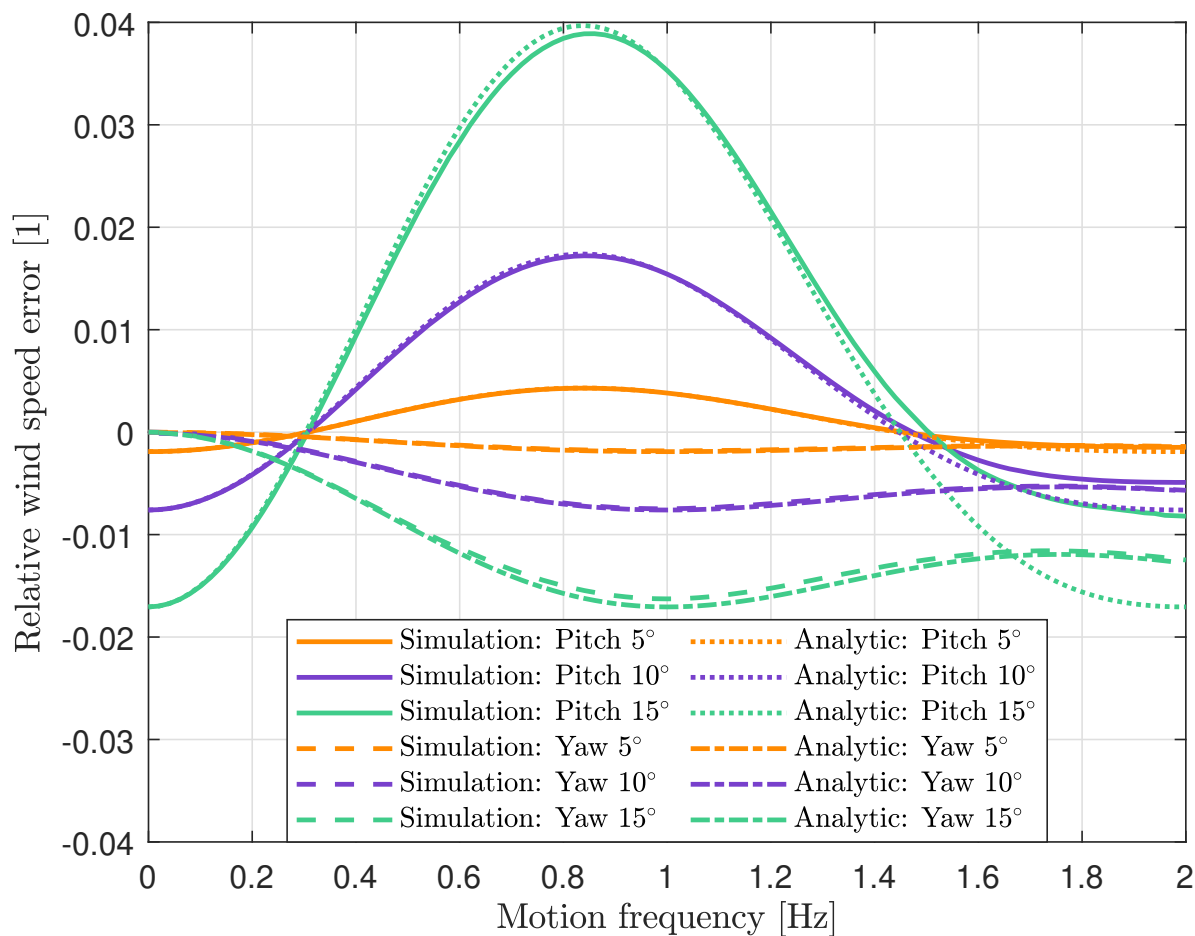
**Figure 6.** Relative motion-induced measurement error caused by pitch (solid) and yaw (dashed) motion as function of oscillation frequency $f_p$ for three arbitrary amplitudes of motion $\alpha = 5°, 10°,$ and $15°$ in absence of wind shear.

## 2.6 Roll motion with no wind shear

Roll motion of a FLS in the absence of wind shear is equivalent to rotating a uniform wind field around an axis parallel to the wind direction. It is therefore intuitive that in the absence of wind shear, FLS motion in roll direction has zero influence on the measurement accuracy. It is not further described here.

205 ## 2.7 Yaw motion

Figure 6 shows the motion-induced error on estimates of horizontal mean wind speed caused by yaw motion, i.e., rotation of the FLS around the vertical axis. It can be seen that the error is zero for slow motion. This is an important finding because the

restoring forces for yaw motion of a FLS are usually low which leads to resulting motion frequencies being also low. We will therefore disregard the effect of yawing in the following.

## 2.8 Pitch motion under the influence of wind shear

The calculations presented above are based on constant wind velocities at all elevations. However, real measurements are usually influenced by a non-zero vertical wind speed gradient, i.e., wind shear. Thus, the influence of wind shear is included by introducing power law wind profiles that are characterized by the wind shear coefficient

$$\alpha = \frac{\log(U_1/U_0)}{\log(z_1/z_0)} \tag{4}$$

where $U_1$ and $U_0$ are the mean wind velocities at elevations $z_1$ and $z_0$ above sea level.

Figure 7 shows the results for measurements for fifteen different wind shear coefficients between 0 and 0.15. Overall, it can be seen that the inclusion of wind shear leads to a reduction of lidar-estimated mean wind speed. The stronger the wind shear, the stronger this effect. This is explained by the scanning geometry. According to

$$\frac{\cos(30° + \varphi) + \cos(30° - \varphi)}{2\cos(30°)} < 0 \tag{5}$$

the average measurement elevation is reduced when the pitch angle $\varphi$ is centered around zero. This can also be seen in Figure 4 (**b**) and (**c**). The reduction of measurement elevation for increased zenith angles is more pronounced than the increase of measurement elevation for decreased zenith angles. The on average reduced measurement elevations due to the effect of pitching lead to reduced mean wind speed estimates in the presence of wind shear profiles with lower wind speeds at lower elevations. The analytic model presented in Appendix A contains a solution for pitch and shear (A3). Its results are plotted in Figure 7 as dashed lines.
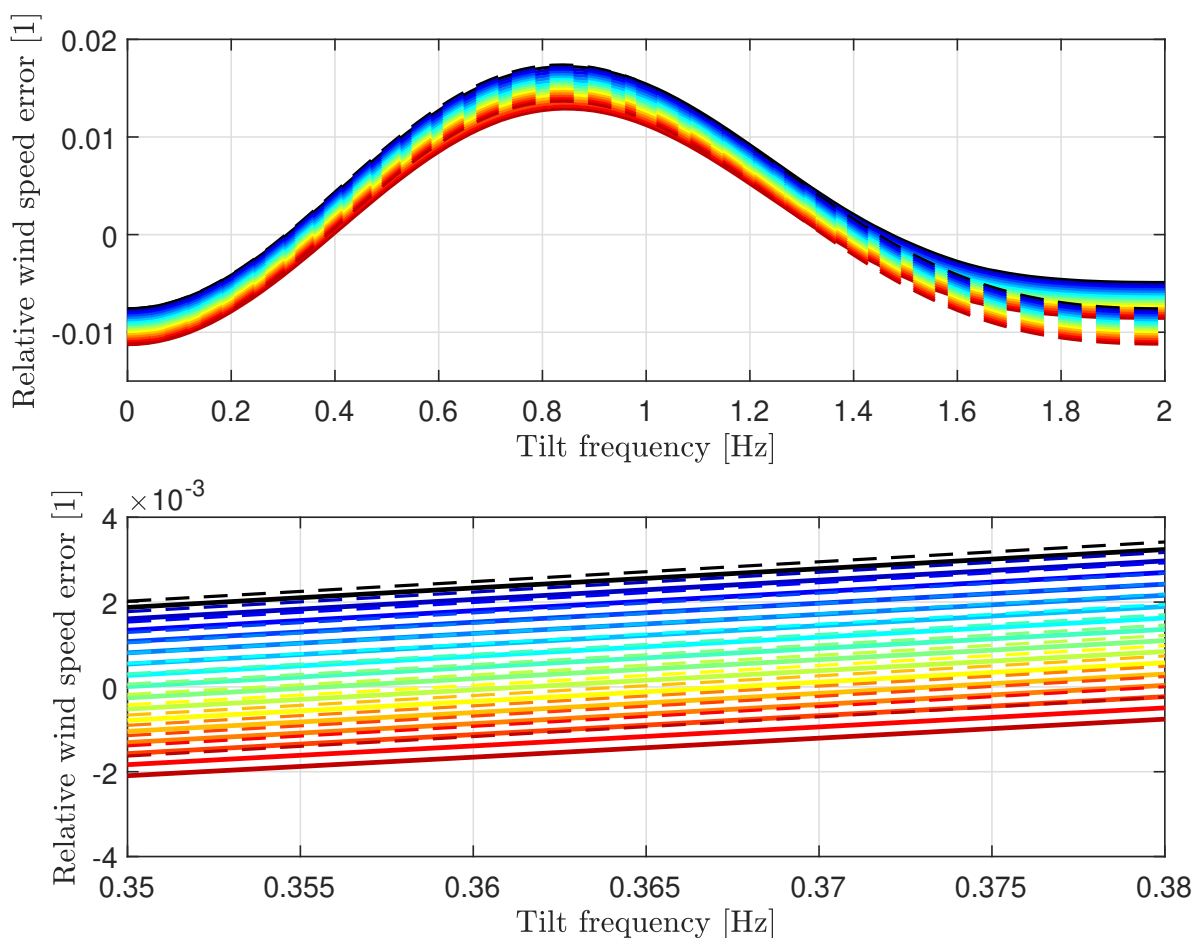
**Figure 7.** (**Top**) Relative motion-induced measurement error caused by pitch motion as function of oscillation frequency $f_p$ for amplitude of motion $A = 10°$ without (black) and with (color) consideration of wind shear characterized by shear coefficients $\alpha = 0.01$ (blue) to $0.15$ (red). Results from simulation (solid) and analytic solution (dashed). (**Bottom**) Enlarged visualization of plot above for $0.35 <= f_p <= 0.38$.

## 2.9 Roll motion under the influence of wind shear

Roll motion influences the elevation of the lidar beams pointing transversal to the inflow wind direction. Since the average elevation is reduced according to Eq.5, we expect some decrease in measured mean wind speed in sheared wind fields. Figure 8 shows that the effect is independent of the motion frequency. The bias caused by roll motion is significantly lower than the
230 effect of pitch motion. Obviously, as in the case of pitch motion, the error caused by roll motion is larger for larger wind shear coefficients. The analytic solution presented in A4 leads to the same results as the simulation.
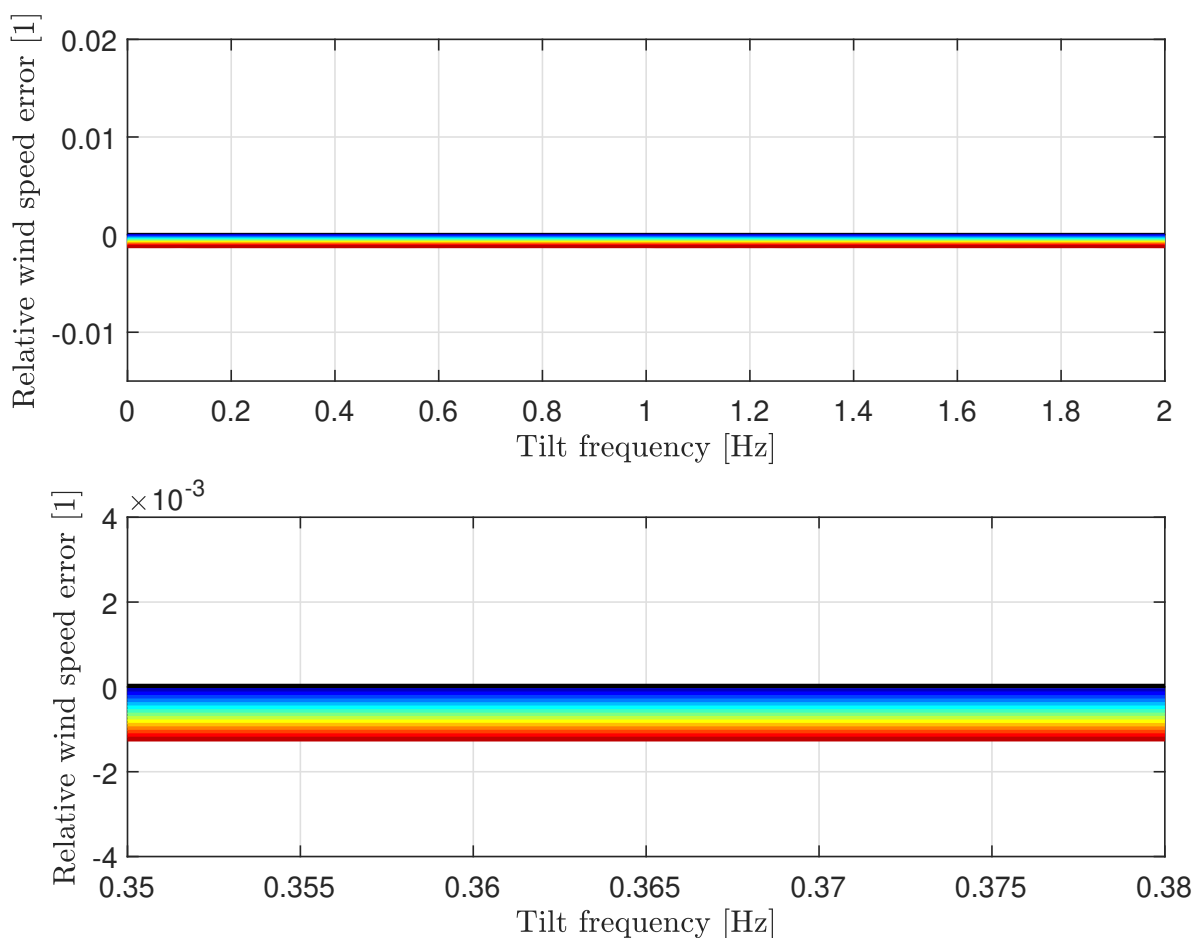
**Figure 8.** (**Top**) Relative motion-induced measurement error caused by roll motion as function of oscillation frequency $f_p$ for amplitude of motion $A = 10°$ without (black) and with consideration of wind shear characterized by shear coefficients $\alpha = 0.01$ (blue) to 0.15 (red). (**Bottom**) Enlarged visualization of plot above for $0.35 <= f_p <= 0.38$.

## 2.10 Measurement elevation

The configuration of measurement heights of the VAD scanning profiling wind lidar influences at which focus distances from the lidar unit a FLS takes measurements. This determines the elevations above sea level at which the radial wind velocities are sampled. Tilt motion modifies the measurement elevations as shown in Figure 4 (**c**). If the vertical gradient of horizontal mean wind speed is zero (i.e., no wind shear), the varying elevation itself has no effect on the LoS velocities. Though, in a sheared wind speed profile with usually higher wind speeds at higher elevations, the changes in elevation have an influence on the mean wind speed results as shown in Figures 7 and 8. In this study, we assume power-law wind shear profiles. For

such shear profiles it is defined that a change in vertical elevation from $z_0$ to $z_1$ by the factor $k_z = \frac{z_1}{z_0}$ leads to a change in
horizontal mean wind speed from $U_0$ to $U_1$ by a factor $k_U = k_z{}^\alpha$. That means that the relative wind speed error caused by
variations of the measurement elevations is independent of the initial elevation $z_0$. It is therefore correct that the lidar simulator
computes identical relative wind speed errors for all measurement heights. For wind shear profiles that follow the power-law
the measurement error is independent of the measurement elevation. This would not be the case for other shear profiles.

## 3 Quantifying the motion-induced measurement error of the SEAWATCH Wind LiDAR Buoy

Section 2.3 shows that the motion-induced measurement bias depends on frequency and amplitude of tilt motion, as well as
the wind shear coefficient. In order to quantify the measurement error for a real FLS application we will in the following
determine realistic values for these three significant parameters. The SWLB is used in this study as an example of a frequently
used commercial FLS.

### 3.1 Tilt frequency

The main driver of motion-induced measurement errors of FLS is tilt motion projected onto the mean wind direction (i.e. here
pitch motion). It was found that the frequency with which pitch motion occurs influences the total measurement error. Luckily,
the tilt frequency of the SWLB is restricted to a narrow band as a Fourier transformation of a tilt signal reveals. Figure 9 shows
the single-sided power spectrum of a period of IMU-measured tilt motion data. The red curve shows the binned averages of
the spectral values. It can be seen that the spectrum has its maximum at 0.365 Hz which corresponds to approximately 2.74 s
tilt period. The bottom plot shows an excerpt of the underlying time series of tilt signal data. The vertical lines are spaced by
2.74 s. The plot is an example of the fairly harmonic shape of the tilt oscillations that are characteristic for the SWLB FLS type
independent of varying amplitudes of motion. We will therefore set 0.365 Hz as the standard frequency for tilt motion of the
SWLB.
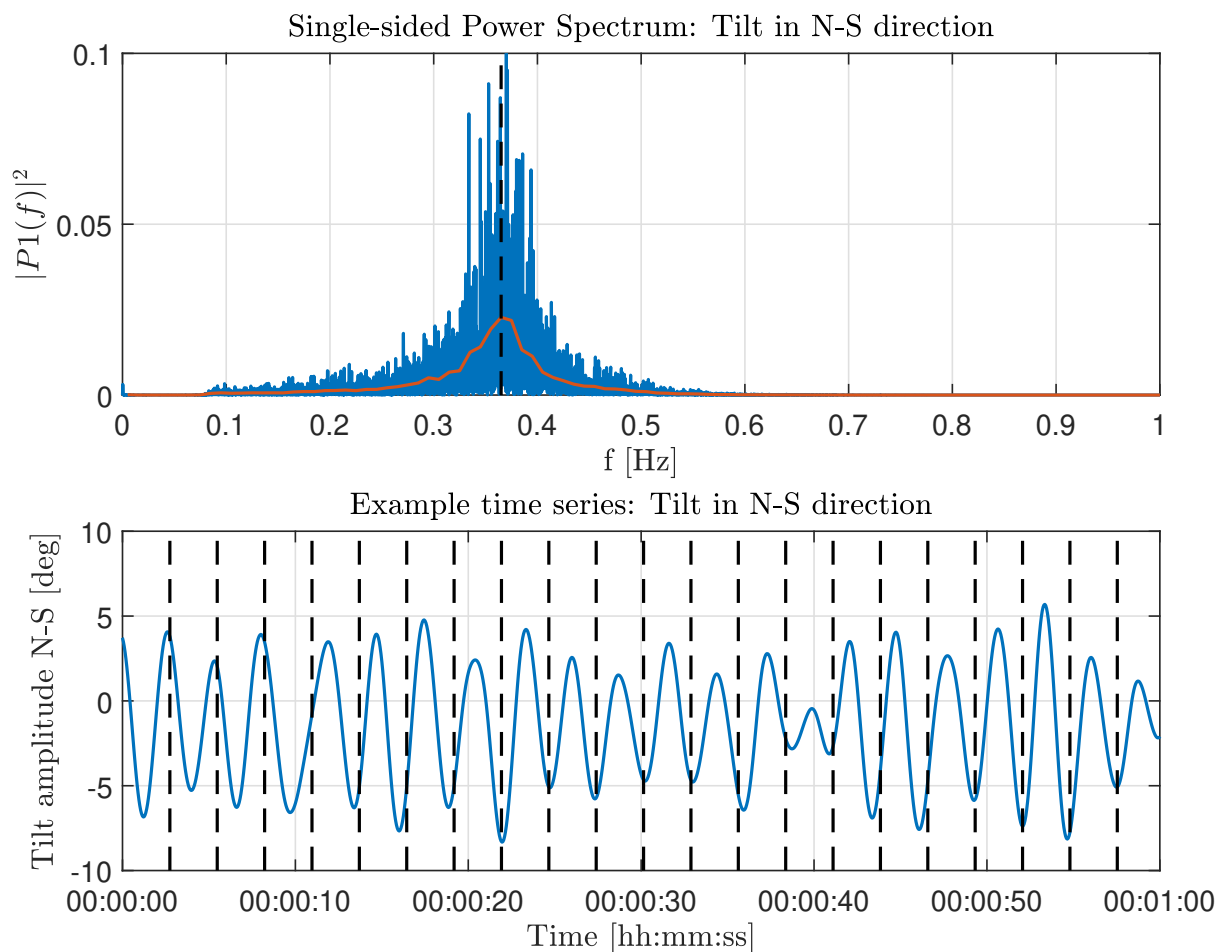
**Figure 9.** (**Top**) Single-sided power spectrum of buoy tilt motion based on IMU measurement data from a SEAWATCH Wind LiDAR Buoy (blue) with bin-averaged spectral values (red). Vertical dashed line marking spectral peak at 0.365 Hz. (**Bottom**) Excerpt of motion data in time domain with vertical dashed lines marking 2.74s (0.365 Hz) long intervals.

### 3.2 Tilt amplitudes

260    The amplitude of tilt motion of a FLS depends on the prevailing sea state. For very calm seas little dynamic tilt motion is expected. By contrast, strong waves will lead to large excitation of the floating platform. The significant wave height is a well-suited parameter to describe the roughness of the sea. Significant wave height as measured by the SWLB is the average wave height, from trough to crest, of the highest third of waves within an interval of approximately 17 minutes.

For determining realistic test conditions, we analyzed measurement data from three long-term measurement campaigns in

265    the North Sea and chose an approximately 4-month long deployment at the East Anglia One meteorological mast (UK), that

showed the highest mean significant wave heights of the four trials considered. Figure 10 shows a histogram of the observed wave heights. The mean of all significant wave heights is approximately 1.1m and the 90th percentile is found at approximately 2.0m. We will consider these wave heights the "normal" and the "strong" wave cases respectively.
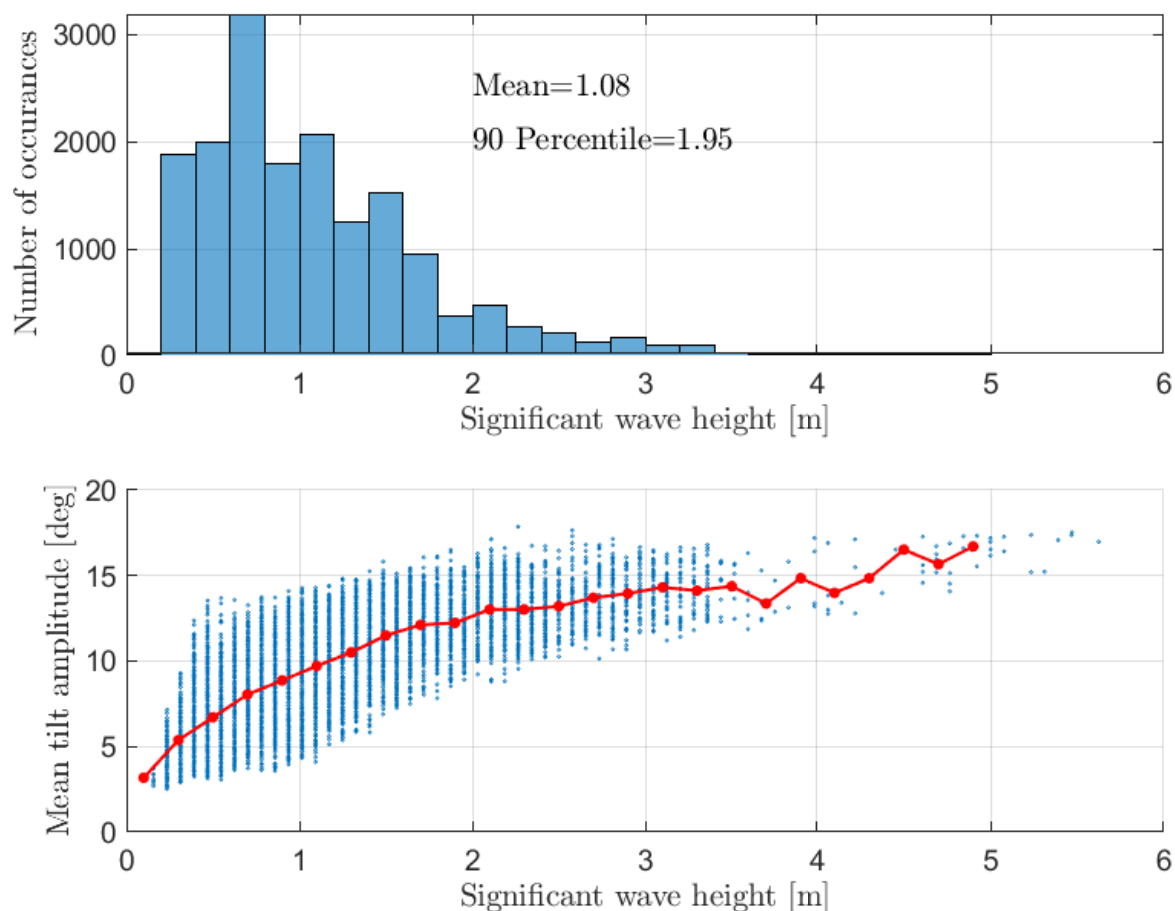
**Figure 10.** (**Top**) Histogram of significant wave heights experienced during an offshore trial of the SWLB at East Anglia One met mast from March through August 2016. Mean and 90th percentile significant wave height listed in the plot. (**Bottom**) Scatter plot of mean tilt amplitude and significant wave height (blue) including mean tilt amplitude binned by significant wave heights (red).

For a specific FLS type the significant wave height has to be transferred to a correlated amplitude of tilt motion to be able
270  to calculate the motion-induced measurement error. This was done in the lower plot of Figure 10. The blue scatter shows data pairs of significant wave height and mean tilt amplitude of the SWLB. While the significant wave height is estimated once every 10 minutes by the FLS's internal data processing, the mean tilt amplitude is calculated for this study. The mean tilt amplitude is the average of the local maxima of the rectified tilt time series. The red curve shows the bin-averaged relationship

between significant wave height and mean tilt amplitude. It can be seen that tilt amplitudes of approximately $10°$ and $12.5°$
275 are expected from the "normal" and "strong" wave cases of 1.1m and 2.0m respectively. These tilt amplitudes can occur in
any direction with regard to the mean wind direction and the relation between wind and wave direction is site-specific. In the
following we will allocate the tilt amplitudes entirely to the pitch DoF. If the quantification of the motion-induced error should
have been performed for a certain deployment instead of a general test case, the tilt motion could have been projected onto the
mean wind vector and tilt in pitch and roll directions could have been handled separately.

### 280 3.3 Wind shear

Usually mean wind velocities increase with vertical distance from the ground due to decreasing influence of surface roughness.
The wind shear exponent $\alpha$ is calculated according to Eq. 4 from the mast-measured horizontal mean wind speeds at 80m and
103m above sea level.

Figure 11 is based on the same measurement data from East Anglia One that we used to determine the correlation between
285 wave height and tilt amplitude. It shows how the significant wave height is correlated with the wind shear exponent. A trend can
be seen towards stronger wind shear exponents for higher waves, likely because higher waves constitute a rougher surface for
the boundary layer. According to the binned averages shown in red in the Figure, we set the wind shear exponent for "normal"
waves to $\alpha = 0.08$ and for "strong" waves to $\alpha = 0.13$.
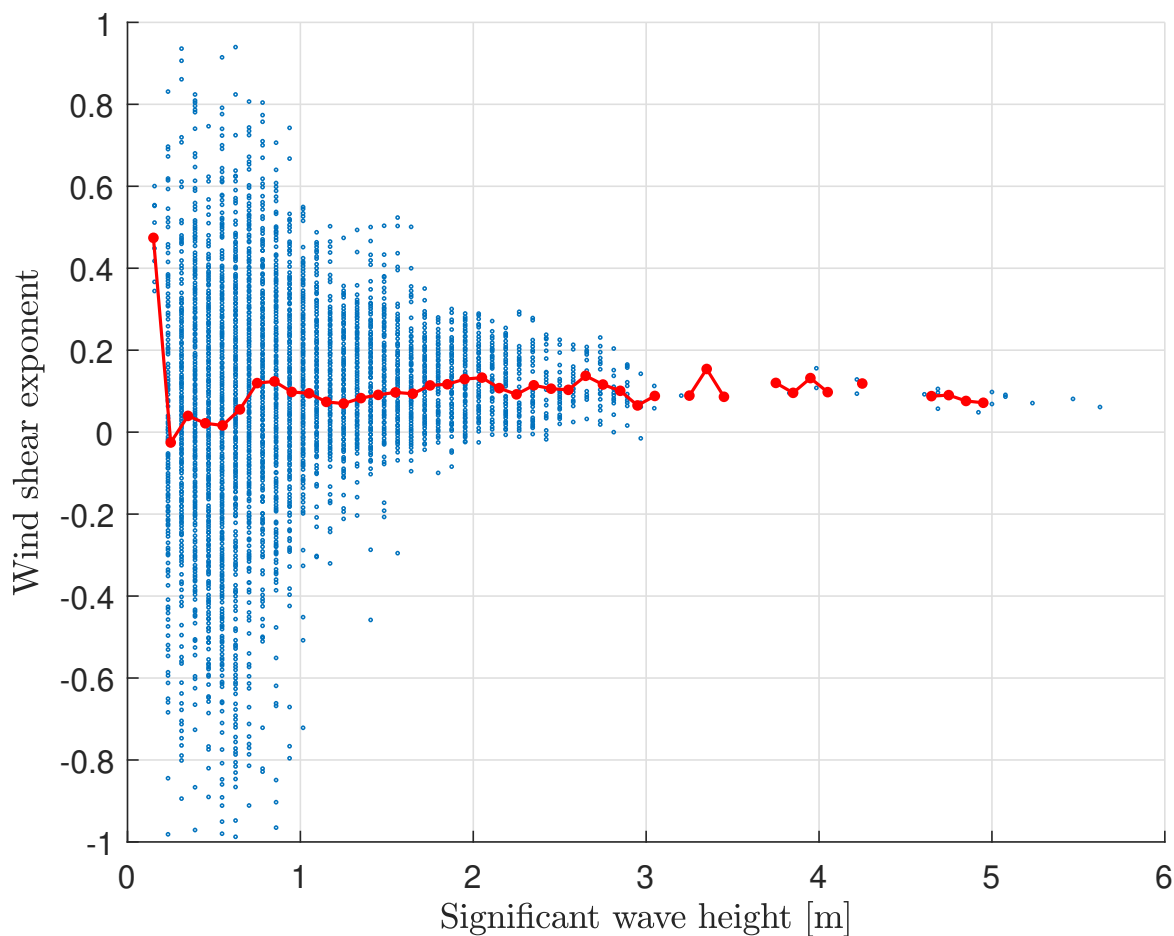
**Figure 11.** Scatter plot of wind shear exponent over significant wave height (blue) and wind shear exponent binned by significant wave height (red).

### 3.4 Results

290   Table 2 summarizes the two test cases that are representative for the SWLB under "normal" and "strong" wave conditions. It also gives the resulting bias values. Both values are very low. Under "normal" wave conditions, we expect the FLS to measure values that are 0.04% higher than what a fixed lidar of the same type would measure. During episodes of "strong" waves it would underestimate the real wind speed by 0.14%.

**Table 2.** Summary of two test cases including the resulting measurement bias for SWLB operating under such typical offshore conditions.

| Case | Tilt frequency | Tilt amplitude | Shear coefficient | Measurement bias |
|---|---|---|---|---|
| "Normal" waves | 0.365 Hz | 10.0° | 0.08 | 0.04% |
| "Strong" waves | 0.365 Hz | 12.5° | 0.13 | -0.14% |

## 4 Discussion and conclusions

295 Computer simulations that imitate the spatio-temporal sampling pattern of a VAD scanning FLS are performed to quantify the motion-induced error on estimates of horizontal mean wind speed. The rotational frequency of the lidar prism is set to 1 Hz which corresponds to the sampling frequency of the ZX 300M lidar type by ZX Lidars, UK that is frequently used on current FLS. It is shown that the relative angle between tilt motion and inflow wind direction is important. We defined tilt motion in wind direction as pitch motion and tilt motion perpendicular to the wind direction as roll motion.

300 For pitch motion, the measurement error is strongly dependent on amplitude and frequency of motion. It is intuitive that small amplitudes of motion lead to less motion-induced error than larger amplitudes. It is shown that FLS that oscillate with very low tilt frequencies close to 0 Hz underestimate wind speeds, while tilt frequencies close to a maximum at around 0.84 Hz lead to overestimated horizontal wind speeds. Close to 0.3 Hz the measurement error is approximately zero if no wind shear is assumed. The presence of positive wind shear, i.e., higher wind speeds at higher elevations, leads to a reduction of the FLS

305 estimates of mean wind speed. The ideal motion frequency that results in zero measurement error lies therefore slightly above 0.3 Hz when wind shear is considered.

For the roll DoF, the motion-induced error is only dependent on the tilt amplitude and the wind shear coefficient. We estimated the error caused by yaw motion to be negligible because its frequency is low for usual FLS.

With the aim of quantifying the motion-induced error for a real FLS, we used experimental data from a Fugro SEAWATCH

310 Wind LiDAR Buoy to determine two test cases. For the case of "normal" wind and wave conditions for a deployment on the North Sea, the amplitude of tilt motion and the wind shear coefficient were set to $10°$ and $\alpha = 0.08$ respectively. A second case representing "strong" wave conditions was defined by $12.5°$ and $\alpha = 0.13$ accordingly. The hydrodymamic properties of the SWLB lead to a dominant tilt frequency of 0.365 Hz which appears to be ideal for mean wind speed measurements with the ZX 300M used on the buoy. The resulting measurement errors for the "normal" and "strong" test cases are 0.04% and

315 -0.14% respectively. These measurement errors are more than an order of magnitude smaller than the uncertainties that are usually found when FLS are validated against meteorological masts. It is therefore difficult to confirm the simulation results during field campaigns. Classification trials however have shown that the sensitivity of measurement error of the SWLB to motion and sea-state parameters is insignificant. And the simulations presented here give a complete explanation for why the motion-induced error is so small.

320     Different approaches could be followed to achieve a compensation of the effect of motion on mean wind speed estimates. These motion-compensation algorithms are hard to assess because their effect would be small compared to the uncertainties in a test setup.

    In this study we did not analyze the random error caused by motion, although this would have been possible for particular test cases based on data from the simulations. The reason is that the random error is strongly dependent on the number of
325 reconstructed wind vectors per averaging interval. For CW wind lidars like the ZX 300 series, the number of reconstructed wind vectors per interval depends on the number of configured and mandatory measurement elevations as well as the amount of filtered data due to adverse atmospheric conditions. In addition, in practical applications, the random error visible as scatter on regression plots also depends on the distance between FLS and reference instrument and the overall uncertainty of FLS and reference instrument. The investigated systematic bias appears to be the most important parameter because it has the potential
330 to influence the slope and offset of linear regression lines as used when e.g., the assessment procedures described in the Carbon Trust Roadmap (Carbon Trust, 2018) are followed.

    The ZX 300 wind lidar with current firmware performs VAD scans with a prism frequency of one rotation per second. Wind vectors are reconstructed based on line-of-sight data from one prism rotation. This study confirms results from field experiments that show that the measurement accuracy of FLS carrying a ZX 300 lidar is comparable to the performance of
335 fixed lidar systems if the frequency of tilt motion is reasonably close to 0.365 Hz. For floating platforms with significantly different hydrodynamic properties that lead to different rotational frequencies and amplitudes, the expected measurement error can be approximated from Figures 7 and 8. For lidar types with a different scanning strategy, similar simulations would need to be performed to determine the systematic measurement deviation.

    Having confirmed that the systematic motion-induced bias on current FLS is low it remains to be investigated in how far
340 lidar motion influences lidar internal data processing routines with regard to data filtering and cloud detection. These could add a different dimension of uncertainty caused by motion.

## Appendix A: Analytic modelling of buoy mean bias

For the analytic approach we assume that the line-of-sight velocities $v_r(\theta')$ are given as a continuous function of the nominal azimuth angle $\theta'$ which is a sound assumption given that the lidar performs 50 measurements per round. The horizontal wind
345 vector $\boldsymbol{U}_l = (U_l, V_l)$ is calculated from the these line-of-sight velocities by

$$U_l \sin\phi = B = \frac{1}{\pi} \int_0^{2\pi} v_r \cos\theta' d\theta' \tag{A1}$$

$$V_l \sin\phi = C = \frac{1}{\pi} \int_0^{2\pi} v_r \sin\theta' d\theta' \tag{A2}$$

where $\phi$ is the half-opening angle and the argument $\theta'$ of $v_r$ is understood. We now assume without loss of generality that the wind is aligned with first axis $\boldsymbol{U} = (U, 0)$. Then $C/B$ is small and the length of the lidar estimated wind vector is

$$
\begin{aligned}
|\boldsymbol{U}_l| &= \frac{B}{\sin\phi}\sqrt{1 + \left(\frac{C}{B}\right)^2} \\
&\approx \frac{1}{\sin\phi}\left(B + \frac{1}{2}\frac{C^2}{B}\right)
\end{aligned}
\tag{A3}
$$

**A1 Pitch only**

The pitch angle $\varphi$ undergoes a harmonic variation as a function of time

$$
\varphi = A\cos(\omega_\varphi(t - t_0))
\tag{A4}
$$

where $A$ is the amplitude, $\omega_\varphi$ is oscillation frequency and $t_0$ is arbitrary initial time. The beam direction of a fixed lidar is

$$
\boldsymbol{n} = \begin{pmatrix} \sin\phi\cos\omega t \\ \sin\phi\sin\omega t \\ \cos\phi \end{pmatrix}
\tag{A5}
$$

where the cyclic frequency is typically 1 Hz, so $\omega \approx 2\pi \text{ s}^{-1}$. The actual beam direction is $\boldsymbol{Mn}$ where the rotation matrix is given by

$$
\boldsymbol{M} = \begin{pmatrix} \cos\varphi & 0 & \sin\varphi \\ 0 & 1 & 0 \\ -\sin\varphi & 0 & \cos\varphi \end{pmatrix}
\tag{A6}
$$

The beam direction of the floating lidar is thus $\boldsymbol{Mn}$ so the line-of-sight velocity is

$$
\begin{aligned}
v_r &= \boldsymbol{U} \cdot \boldsymbol{Mn} \\
&= U\left[\sin\phi\cos\omega t\cos(A\cos(\omega_\varphi(t - t_0))) + \cos\phi\sin(A\cos(\omega_\varphi(t - t_0)))\right]
\end{aligned}
\tag{A7}
$$

or, if we define $\chi = \omega_\varphi/\omega$, $\theta' = \omega t$ and a random initial phase $\phi_r = \omega_\varphi t_0$, it can be written as

$$
v_r = U\left[\sin\phi\cos\theta'\cos(A\cos(\chi\theta' - \phi_r)) + \cos\phi\sin(A\cos(\chi\theta' - \phi_r))\right]
\tag{A8}
$$

The ensemble average of $B$ is obtained by averaging over all random phases $\phi_r$:

$$
\langle B\rangle = \frac{1}{2\pi^2}\iint\limits_0^{2\pi} v_r\cos\theta'\, d\theta'\, d\phi_r
\tag{A9}
$$

Inserting $v_r$ from (A8) and interchanging the order of integration one gets

$$
\begin{aligned}
\langle B\rangle &= \frac{U}{\pi}\int\limits_0^{2\pi}\sin\phi\cos^2\theta'\, J_0(A)\, d\theta' \\
&= U\sin\phi\, J_0(A)
\end{aligned}
\tag{A10}
$$

370 where $J_0(A)$ is the Bessel function of the first kind. This means that the average wind component in the mean wind direction can be estimated as

$$U = \frac{\langle B \rangle}{\sin \phi \, J_0(A)} \tag{A11}$$

and where the bias correction $J_0(A)$ depends on the amplitude $A$ but not the non-dimensional frequency $\chi$.

Equation (A3) says that the random variations in the transverse wind speed contributes to the average of the horizontal wind

375 vector. The average of $C$ is zero but the variations around zero have to be calculated. The average of $C^2$ is calculated by multiplying the right hand side of (A2) with itself, substituting $\theta' \to \theta''$ in one of the integrals and converting the product into a double integral. This is finally averaged over $\phi_r$ to get

$$\langle C^2 \rangle = \frac{1}{2\pi^3} \int\!\!\!\int\!\!\!\int_0^{2\pi} v_r(\theta') v_r(\theta'') \sin \theta' \sin \theta'' d\theta' d\theta'' d\phi_r$$

$$= \frac{U^2}{2\pi^3} \int\!\!\!\int\!\!\!\int_0^{2\pi} [\sin \phi \cos \theta' \cos(A\cos(\chi\theta' + \phi_r)) + \cos \phi \sin(A\cos(\chi\theta' + \phi_r))]$$

380
$$\times [\sin \phi \cos \theta'' \cos(A\cos(\chi\theta'' + \phi_r)) + \cos \phi \sin(A\cos(\chi\theta'' + \phi_r))]$$

$$\times \sin \theta' \sin \theta'' d\theta' d\theta'' d\phi_r \tag{A12}$$

The idea now is to assume $A$ is small so that the trigonometric functions containing $A$ can be expanded to second order as $\cos x \approx 1 + x^2/2$ and $\sin x \approx x$. It can be shown that using this expansion, the only term left after expanding the product between the two parentheses in (A12) is the product between the $\sin(A...)$ terms. Retaining terms of second order in $A$ one

385 gets

$$\langle C^2 \rangle = \frac{U^2}{2\pi^3} \int\!\!\!\int\!\!\!\int_0^{2\pi} A^2 \cos^2 \phi \cos(\chi\theta' + \phi_r) \cos(\chi\theta'' + \phi_r) \sin \theta' \sin \theta'' d\phi_r d\theta' d\theta'' \tag{A13}$$

where we have also changed the order of integration. The integration over $\phi_r$ results in

$$\langle C^2 \rangle = \frac{A^2 U^2 \cos^2 \phi}{2\pi^2} \int\!\!\!\int_0^{2\pi} \cos(\chi(\theta' - \theta'')) \sin \theta' \sin \theta'' d\theta' d\theta''$$

$$= \frac{A^2 U^2 \cos^2 \phi}{\pi^2} \frac{2 \sin^2(\pi\chi)}{(1-\chi^2)^2} \tag{A14}$$

390 Averaging (A3),

$$\langle |\boldsymbol{U}_l| \rangle \approx \frac{1}{\sin \phi} \left( \langle B \rangle + \frac{1}{2} \frac{\langle C^2 \rangle}{\langle B \rangle} \right) \tag{A15}$$

and substituting (A10) for the average of $B$ and (A14) for the average of $C^2$ in this equation, we finally get

$$\langle |\boldsymbol{U}_l| \rangle \approx U \left[ J_0(A) + \frac{A^2}{J_0(A)} \frac{\cot^2 \phi}{\pi^2} \frac{\sin^2(\pi\chi)}{(1-\chi^2)^2} \right] \quad . \tag{A16}$$

## A2 Yaw only

395 The impact of harmonic yaw oscillations on the mean wind speed can be calculated in almost exactly the same way. Here the rotation matrix (A6) will become

$$
\boldsymbol{M} = \begin{pmatrix} \cos\varphi & \sin\varphi & 0 \\ -\sin\varphi & \cos\varphi & 0 \\ 0 & 0 & 1 \end{pmatrix} \tag{A17}
$$

and the only modification to $v_r$ in (A8) will be that in the second term $\cos\phi$ will be changed to $\sin\phi\sin\theta'$. Following the same steps as in section A1 one arrives to

400 $$\langle|\boldsymbol{U}_l|\rangle \approx U\left[J_0(A) + \frac{4A^2}{J_0(A)}\frac{1}{\pi^2}\frac{\sin^2(\pi\chi)}{(\chi^3 - 4\chi)^2}\right] \quad . \tag{A18}$$

## A3 Pitch and shear

If the wind is not constant with height our results might change. Here we assume that the wind profile can be described by a power law profile with an exponent $\alpha$, see Eq. 4. It is well known that the the curvature of the wind profile is important for the bias when averaging over a range of heights. However, here it turns out that the curvature is of small importance relative to the 
405 gradient. Anyway, we expand the wind profile to second order

$$
U(z) \approx U_0\left(1 + \alpha\frac{\Delta z}{z_0} + \frac{\alpha(\alpha-1)}{2}\left(\frac{\Delta z}{z_0}\right)^2\right) \tag{A19}
$$

in order to see this small dependence on the second order in $\Delta z/z_0$. Using Eqs. A5 and A6, the relative height difference becomes

$$
\frac{\Delta z}{z_0} = \frac{(\boldsymbol{Mn})_3}{n_3} - 1 = \cos(A\cos(\chi\theta' - \varphi_r)) - \cos\theta'\sin(A\cos(\chi\theta' - \varphi_r))\tan\phi - 1 \tag{A20}
$$

410 utilizing the notation of Eq. A8. We now substitute Eq. A19 into Eq. A9 and expand all terms, integrate with respect to $\varphi_r$, and then with respect to $\theta'$. The result is

$$
\begin{aligned}
\frac{\langle B\rangle}{\sin\phi} = U_0\bigg( & J_0(A) - \alpha\left[J_0(A) - J_0(2A)\right] \\
& + \frac{\alpha(\alpha-1)}{32}\left[J_0(A)(20 + 3\tan^2\phi) - 32J_0(2A) + 3J_0(3A)(4 - \tan^2\phi)\right]\bigg)
\end{aligned} \tag{A21}
$$

and the term with $\alpha(\alpha-1)$ is typically insignificant relative to the term with $\alpha$ corresponding to the influence of the second and first derivative of the wind profile, respectively. When $\alpha = 0$ we are left with the result Eq. A10. When $\alpha = 1$, that is $U \propto z$ 
415 the last term vanishes and $\langle B\rangle/\sin\phi = U_0J_0(2A)$.

We now need to see if $C$ is affected by shear. If $A$ is small, then the relative height difference can be written as

$$
\frac{\Delta z}{z_0} \approx -A\tan\phi\cos\theta'\cos(\chi\theta' - \varphi_r) - \frac{A^2}{2}\cos^2(\chi\theta' - \varphi_r) \tag{A22}
$$

applying the same argumentation that led from Eq. A12 to Eq. A13. Using this it can be shown that the shear induced terms are third order in $A$ and are therefore dropped. The final result is thus Eq. A15 using Eq. A14 for $\langle C^2\rangle$ and Eq. A21 for $\langle B\rangle$.

## A4 Roll and shear

In a yaw only situation, the shear will not change the line-of-sight velocity because the measurement height remains constant. Neither the roll motion in a constant wind profile will alter the line-of-sight velocity because roll will not change the along wind component of the beam unit vector. Therefore we investigate the impact of shear combined with roll. The rotation matrix corresponding to roll motion is

$$\boldsymbol{M} = \begin{pmatrix} 1 & 0 & 0 \\ 0 & \cos\varphi & \sin\varphi \\ 0 & -\sin\varphi & \cos\varphi \end{pmatrix} \tag{A23}$$

where $\varphi$ is still given by Eq. A4 but $\varphi$ now means the roll angle. Since this matrix does not change the first component of the pointing vector $\boldsymbol{n}$ it is only the change in measurement height that will alter $v_r$. In parallel with Eq. A20 we can now calculate the relative height change of the focus position:

$$\frac{\Delta z}{z} = \frac{(\boldsymbol{Mn})_3}{n_3} - 1 = \cos(A\cos(\chi\theta' - \varphi_r)) - \sin\theta'\sin(A\cos(\chi\theta' - \varphi_r))\tan\phi - 1 \tag{A24}$$

Just using up to the first order in the expansion of the wind profile Eq. A19, the average of $B$ becomes

$$\langle B \rangle = \frac{1}{2\pi^2} \int\!\!\!\int_0^{2\pi} v_r \cos\theta' d\varphi_r d\theta'$$

$$= \frac{U_0 \sin\phi}{2\pi^2} \int\!\!\!\int_0^{2\pi} \left(1 + \alpha\frac{\Delta z}{z}\right) d\varphi_r \cos^2\theta' d\theta'$$

Now we substitute the relative height difference Eq. A24 and integrate first over $\varphi_r$ and then over $\theta'$ to get

$$\langle B \rangle = \frac{U_0 \sin\phi}{\pi} \int_0^{2\pi} (1 + \alpha(J_0(A) - 1)) \cos^2\theta' d\theta'$$

$$= U_0 \sin\phi \, (1 + \alpha(J_0(A) - 1)) \tag{A25}$$

Taking into account the curvature of the wind profile, i.e. the second order term in Eq. A19, does not change the result significantly meaning that the already small correction is changed less than 10%. For completeness we give the expression

$$\langle B \rangle = U_0 \sin\phi \left[ 1 + \alpha(J_0(A) - 1) + \right.$$

$$\left. \frac{\alpha(\alpha - 1)}{2} \left( 1 - 2J_0(A) + \frac{1 + J_0(2A)}{2} + \frac{1 - J_0(2A)}{8}\tan^2\phi \right) \right] \tag{A26}$$

To complete the impact of roll and shear on the average lidar speed we need, according to Eq. A15, to calculate $\langle C^2 \rangle$. Following
the discussion after Eq. A23 and expanding only to first order in $\Delta z / z$ the line-of-sight velocity becomes

$$v_r = \boldsymbol{U} \cdot \boldsymbol{M}\boldsymbol{n} = U(z) \sin\phi \cos\theta'$$
$$\approx U_0 \left(1 + \alpha \frac{\Delta z}{z}\right) \sin\phi \cos\theta' \tag{A27}$$

Using this equation and Eq. A12, $\langle C^2 \rangle$ can be written as

$$\langle C^2 \rangle = \frac{U_0^2 \sin^2\phi}{2\pi^3} \iiint\limits_0^{2\pi} \left(1 + \alpha\frac{\Delta z'}{z}\right)\left(1 + \alpha\frac{\Delta z''}{z}\right) d\phi_r \cos\theta' \cos\theta'' \sin\theta' \sin\theta'' d\theta' d\theta'' \tag{A28}$$

Here the primes and double primes on $\Delta z$ correspond to primed or double primed $\theta$'s in Eq. A24. We again use the expansion
of the trigonometric functions in Eq. A24 assuming $A$ is small, so

$$\frac{\Delta z'}{z} \approx \frac{A^2}{2}\cos(\chi\theta' - \varphi_r) - A\sin\theta'\tan\phi\cos(\chi\theta' - \varphi_r) \tag{A29}$$

Expanding the two parentheses inside the triple integral in Eq. A28 gives four terms. The first three are, when integrated over
$\varphi_r$, independent of $\theta'$ and $\theta''$ so the integrals over $\theta'$ and $\theta''$ of those terms give zero. We are left with

$$\langle C^2 \rangle = \frac{\alpha^2 U_0^2 \sin^2\phi}{2\pi^3} \iiint\limits_0^{2\pi} \frac{\Delta z'}{z}\frac{\Delta z''}{z} d\phi_r \cos\theta' \cos\theta'' \sin\theta' \sin\theta'' d\theta' d\theta'' \tag{A30}$$

We now substitute Eq. A29 and retain only terms of up to second order in $A$. The resulting expression is

$$\langle C^2 \rangle = \frac{\alpha^2 A^2 U_0^2 \sin^2\phi\tan^2\phi}{2\pi^3} \iiint\limits_0^{2\pi} \cos(\chi\theta' - \varphi_r)\cos(\chi\theta'' - \varphi_r)d\phi_r \cos\theta' \cos\theta'' \sin^2\theta' \sin^2\theta'' d\theta' d\theta'' \tag{A31}$$

The integral over $\varphi_r$ divided by $\pi$ is $\cos(\chi(\theta' - \theta''))$ so the final expression is

$$\langle C^2 \rangle = \frac{\alpha^2 A^2 U_0^2 \sin^2\phi\tan^2\phi}{2\pi^2} \iint\limits_0^{2\pi} \cos(\chi(\theta' - \theta''))\cos\theta' \cos\theta'' \sin^2\theta' \sin^2\theta'' d\theta' d\theta''$$
$$= \frac{\alpha^2 A^2 U_0^2 \sin^2\phi\tan^2\phi}{2\pi^2} \frac{16\chi^2 \sin^2(\pi\chi)}{(\chi^2 - 1)(\chi^2 - 9)} \tag{A32}$$

This adjustment is second order in $\alpha$ in contrast to the correction to $\langle B \rangle$ which is first order in $\alpha$. Since the relevant values of $\alpha$
are small and the other terms are also limited in magnitude for relevant parameters, $\langle C^2 \rangle$ can be safely ignored, and the final
expression for the mean speed is

$$\langle |\boldsymbol{U}_l| \rangle \approx \frac{\langle B \rangle}{\sin\phi} = U_0 \left(1 + \alpha(J_0(A) - 1)\right) \tag{A33}$$

where we have used Eq. A25.

*Author contributions.* "FK designed the study, performed the numerical simulations, and prepared the manuscript. JM developed the analytic model and reviewed the manuscript. All authors analyzed the results."

*Competing interests.* Fugro Norway AS is the manufacturer of the SEAWATCH Wind LiDAR Buoy. The author FK is an employee of Fugro
465    Norway AS.

# References

Bischoff, O., Schlipf, D., Würth, I., and Cheng, P. W.: Dynamic Motion Effects and Compensation Methods of a Floating Lidar Buoy, EERA DeepWind 2015 Deep Sea Offshore Wind Conference, https://doi.org/10.7567/JJAP.54.07JA03, 2015.

Bischoff, O., Yu, W., Gottschall, J., and Cheng, P. W.: Validating a simulation environment for floating lidar systems, in: Journal of Physics:
470    Conference Series, vol. 1037, https://doi.org/10.1088/1742-6596/1037/5/052036, 2018.

Carbon Trust: OWA roadmap for the commercial acceptance of floating LiDAR technology, 2018.

DNV GL: Floating Lidar Stage 2 Type Validation DNV GL Type Validation of the ACCURASEA Floating Lidar, https://tinyurl.com/ACCURASEA, 2019.

Désert, T., Knapp, G., and Aubrun, S.: Quantification and correction of wave-induced turbulence intensity bias for a floating lidar system,
475    Remote Sensing, 13, https://doi.org/10.3390/rs13152973, 2021.

Emeis, S., Harris, M., and Banta, R. M.: Boundary-layer anemometry by optical remote sensing for wind energy applications, Meteorologische Zeitschrift, 16, https://doi.org/10.1127/0941-2948/2007/0225, 2007.

Gottschall, J., Courtney, M. S., Wagner, R., Jørgensen, H. E., and Antoniou, I.: Lidar profilers in the context of wind energy-a verification procedure for traceable measurements, Wind Energy, 15, https://doi.org/10.1002/we.518, 2012.

480    Gottschall, J., Wolken-Möhlmann, G., Viergutz, T., and Lange, B.: Results and conclusions of a floating-lidar offshore test, Energy Procedia, 53, https://doi.org/10.1016/j.egypro.2014.07.224, 2014.

Gottschall, J., Gribben, B., Stein, D., and Würth, I.: Floating lidar as an advanced offshore wind speed measurement technique: current technology status and gap analysis in regard to full maturity, Wiley Interdisciplinary Reviews: Energy and Environment, 6, https://doi.org/10.1002/wene.250, 2017.

485    Gutiérrez-Antuñano, M. A., Tiana-Alsina, J., Salcedo, A., and Rocadenbosch, F.: Estimation of the motion-induced horizontal-wind-speed standard deviation in an offshore Doppler lidar, Remote Sensing, 10, https://doi.org/10.3390/rs10122037, 2018.

Hellevang, J. O. and Reuder, J.: Effect of wave motion on wind lidar measurements - Comparison testing with controlled motion applied, in: DeepWind 2013 - 10th Deep Sea Offshore Wind R&D Conference, 2013.

Kelberlau, F. and Mann, J.: Better turbulence spectra from velocity-azimuth display scanning wind lidar, Atmospheric Measurement Tech-
490    niques, 12, https://doi.org/10.5194/amt-12-1871-2019, 2019.

Kelberlau, F., Neshaug, V., Lønseth, L., Bracchi, T., and Mann, J.: Taking the motion out of floating lidar: Turbulence intensity estimates with a continuous-wave wind lidar, Remote Sensing, 12, https://doi.org/10.3390/rs12050898, 2020.

Mangat, M., Roziers, E. B. D., Medley, J., Pitter, M., Barker, W., and Harris, M.: The impact of tilt and inflow angle on ground based Lidar wind measurements, in: European Wind Energy Association Conference and Exhibition 2014, EWEA 2014, 2014.

495    Pitter, M., des Roziers, E. B., Medley, J., Mangat, M., Slinger, C., and Harris, M.: Performance Stability of ZepIR in High Motion Environments: Floating and Turbine Mounted, https://www.zxlidars.com/wp-content/uploads/2014/12/Performance-stability-of-ZephIR-in-high-motion-environments.pdf, 2014.

Rutherford, A., Pitter, M., Slinger, C., des Roziers, E. B., Barker, W., and Harris, M.: The effect of motion on continuous wave lidar wind measurements, in: Windpower 2013, 2013.

500    Salcedo-Bosch, A., Farre-Guarne, J., Sala-Alvarez, J., Villares-Piera, J., Tanamachi, R., and Rocadenbosch, F.: Floating Doppler Wind Lidar Motion Simulator for Horizontal Wind Speed Measurement Error Assessment, in: 2021 IEEE International Geoscience and Remote Sensing Symposium IGARSS, https://doi.org/10.1109/igarss47720.2021.9555023, 2021.

Schlipf, D., Rettenmeier, A., and Haizmann, F.: Model Based Wind Vector Field Reconstruction from LIDAR Data, Proceedings of the 11th German Wind Energy Conference DEWEK, 2012.

505    Smith, D. A., Harris, M., Coffey, A. S., Mikkelsen, T., Jørgensen, H. E., Mann, J., and Danielian, R.: Wind lidar evaluation at The danish wind test site in høvsøre, Wind Energy, 9, https://doi.org/10.1002/we.193, 2006.

Stein, D., Faghani, D., Beeken, A., and Schwenk, P.: Assessment of the Fugro/OCEANOR SEAWATCH Floating LiDAR Verification at RWE IJmuiden met mast, https://tinyurl.com/SWLB0, 2015.

Tiana-Alsina, J., Gutierrez, M. A., Wurth, I., Puigdefabregas, J., and Rocadenbosch, F.: Motion compensation study for a floating

510    Doppler wind LiDAR, in: 2015 IEEE International Geoscience and Remote Sensing Symposium (IGARSS), vol. 2015-November, https://doi.org/10.1109/IGARSS.2015.7327051, 2015.

Wolken-Möhlmann, G. and Gottschall, J.: Dependence of Floating LiDAR performance on external parameters - Are existing onshore classification methods applicable?, Journal of Physics: Conference Series, 1669, https://doi.org/10.1088/1742-6596/1669/1/012025, 2020.

Wolken-Möhlmann, G., Lilov, H., and Lange, B.: Simulation of motion induced measurement errors for wind measurements using LIDAR

515    on floating platforms, Isars 2010, 2010.